Steel-reinforced resin for bolted shear connectors
Confined behaviour under quasi-static cyclic loading

Pedrosa, Bruno; Buecking, L.; Veljkovic, Milan

DOI
10.1016/j.engstruct.2022.114023

Publication date
2022

Document Version
Final published version

Published in
Engineering Structures

Engineering Structures 256 (2022) 114023

Contents lists available at ScienceDirect

Engineering Structures

journal homepage: www.elsevier.com/locate/engstruct

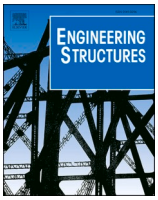

Steel-reinforced resin for bolted shear connectors: Confined behaviour under quasi-static cyclic loading

Bruno Pedrosa [a,*], Linda Bücking [b,1], Milan Veljkovic [b]

[a] University of Coimbra, ISISE, Department of Civil Engineering, Coimbra, Portugal
[b] Faculty of Civil Engineering and Geosciences, Delft University of Technology, Delft, Netherlands

ARTICLE INFO

Keywords:
Steel-reinforced resin
Bolted shear connector
Confined conditions
Linear Drucker-Prager model

ABSTRACT

Injections bolts were initially conceptualized to repair riveted connections in bridges with long service lifetime and now they are widely used in steel and composite structures. Injecting steel-reinforced epoxy resin in bolted connections with oversized holes is a novel approach to enable fast and easy assembly of composite structures while limiting slip between the components. The performance of these bolted shear connectors is mainly dependent on the injected material. In this paper, short-term mechanical properties of an epoxy-based resin mixed with steel shots (steel-reinforced resin) are evaluated to consider it for bolted shear connectors. Uniaxial static tests allowed to compare the stiffness and ductility of resin and steel-reinforced resin and to define a hardening law, while multiaxial tests were conducted under quasi-static cyclic loading in order to characterize the material behaviour under confined conditions. Steel-reinforced resin specimens showed a stiffness under confined conditions 2.6 times higher compared to the bare resin specimens. This increase of stiffness is fundamental to achieve slip resistant behaviour when resin-injected shear connectors are used in significantly oversized holes. The linear Drucker-Prager plastic model was used to define the material behaviour. The good agreement observed indicates that future investigations on numerical and experimental performance of bolted shear connectors can be implemented with the parameters proposed in this paper.

1. Introduction

The concept of an injection bolt was developed in the 1970s as a solution for renovation of faulty riveted connections in metallic bridges. Applying new rivets was not an option since it was no longer a common practice. Additionally, the solution had to withstand reversal cyclic loading, therefore a standard bolted connection can only be applied if bolts were pretensioned. However, the conditions of the faying surfaces (relevant for friction coefficient) are unreliable, generally. In this sense, the challenge was to develop a connection that is slip-resistant and does not rely on friction [1].

An injection bolt is characterized by having the gap between the bolt shank and the hole of the plate completely filled with a resin which is normally injected through a hole in the bolt's head as recommended in Annex K of EN 1090-2 [2]. After the resin has hardened, a slip resistant connection is accomplished. Resin also contributes to reduce the vulnerability of the bolt against corrosion damages [3].

The mechanical behaviour of injection bolts under static loading is similar to fitted bolts but the stiffness of the connection using injection bolts is directly dependent on the mechanical properties of the resin [4]. Any resin can be implemented as far as conditions in EN 1090-2 [2] are fulfilled which are related to its viscosity (ability to fill the cavity), thixotropic behaviour (it should remain in the cavity after injection) and its pot life (minimum 15 min). However, the design bearing strength of an injection bolt is directly dependent on the bearing strength of the resin (Eq. 3.4 of EN 1993-1-8 [5]) which is determined with a normalized test (Annex G of EN 1090-2 [2]). It corresponds to the maximum applied bearing stress considering 0.3 mm as the limit for the displacement during the design life of the structure. In this sense, materials with high stiffness and small creep deformations should be preferable for static design.

RenGel® SW 404 + HY 2404/5159 has been intensively studied and it is the only two component resin that has been approved by the Dutch Ministry of Infrastructures and Water Management [6] to use in injection bolts. Experimental tests proved that this material allows to fulfil the requirements related to the cumulative connection slip at the end of the service life (not more than 0.3 mm) when normalized holes are used

* Corresponding author.
E-mail address: bruno.pedrosa@uc.pt (B. Pedrosa).
[1] Present address: Leibniz University Hannover, Institute of Mechanics and Computational Mechanics, Germany.

https://doi.org/10.1016/j.engstruct.2022.114023
Received 12 July 2021; Received in revised form 12 January 2022; Accepted 11 February 2022
Available online 21 February 2022

Nomenclature

A-Set	Ascending loading set
a	Third invariant of deviatoric stress
c	Material cohesion, Mohr-Coulomb criterion
C3D8R	Linear finite element with 8 nodes and reduced integration
d	Material cohesion, Drucker-Prager model
D-Set	Descending loading set
$d\varepsilon^{pl}$	Plastic strain increment
$d\bar{\varepsilon}^{pl}$	Equivalent plastic strain increment
$E_{conf,i}$	Stiffness under confined conditions at cycle i
E_Z	Young's modulus
$f_{y,c}$	Uniaxial compressive yield strength
$f_{y,t}$	Uniaxial tensile yield strength
F	Applied force
FRP	Fibre-reinforced polymer
G	Flow potential
K	Ratio between triaxial tension and compression yield stresses
L	Specimen's height
L_R	Resin specimen's height
L_{SRR}	Steel-reinforced resin specimen's height
p	Hydrostatic stress
q	von Mises equivalent stress
R	Resin specimen
SRR	Steel-reinforced resin specimen
t	Deviatoric stress
U_r	Radial deformation
β	Material friction angle, Drucker-Prager model
$\varepsilon_r, \varepsilon_h, \varepsilon_z$	Nominal strain in cylindrical coordinates: radial, hoop, axial
$\varepsilon_{z_0}^{f}$	Nominal fracture initiation strain
$\varepsilon_{z,pl}$	Nominal plastic strain
$\varepsilon_{z,r,i}$	Nominal residual strain at cycle i
$\varepsilon_{z,r,pl,i}$	Nominal residual plastic strain at cycle i
$\varepsilon_{z,r,visc,i}$	Nominal residual viscoelastic strain at cycle i
$\sigma_1, \sigma_2, \sigma_3$	Principal stresses, Mohr-Coulomb criterion
$\sigma_r, \sigma_h, \sigma_z$	Nominal stress in cylindrical coordinates: radial, hoop, axial
$\sigma_{z,true}$	Axial true stress
φ	Material friction angle, Mohr-Coulomb criterion
ψ	Material dilatation angle, Drucker-Prager model

[7].

Injection bolts have also been studied for application in hybrid structures (steel-FRP) for innovative light-weight bridges [8–10], in crane girders [11], towers for wind turbines and stadium roofs [7]. Fatigue tests on preloaded injected bolted connections were conducted by several authors showing that there is a contribute to reduce the scatter on the results and to improve the fatigue life [12–15].

However, using resin injections in bolted connections with oversized holes requires additional attention since the load-bearing resin volume is larger and deformations will increase. Such oversized holes are crucial when using resin-injected bolted shear connectors in demountable steel–concrete composite floor systems: Nijgh et al [16,17] conducted scientific investigations on the demountability and reusability of a tapered steel–concrete composite beam whose dimensions replicate typical dimensions of a multi-storey car park building. Demountable resin-injected shear connectors were proposed – see schematic representation in Fig. 1 – using M20 bolts and 32 mm for the diameter of holes in the beam flange. To account for tolerances in the construction process, the hole clearance is 4 times larger than normalized hole dimensions. In accordance with these dimensions, a set of creep tests was conducted by Nijgh [16] using double-lap shear connections with M20 bolts in oversized holes with 32 mm of diameter. Results for a normal bearing stress of 175 MPa are presented in Fig. 2a) and it is possible to observe that by extrapolating results to 50 years, the maximum deformation criterion prescribed in EN 1090-2 (0.30 mm) is not verified for conventional resin while for steel-reinforced resin this requirement is verified. This reinforced solution has been studied at Delft University of Technology [18]. Steel shots are used as the reinforcement of the epoxy resin as they are made of stiffer material – see Fig. 2b). It is expected to achieve higher compressive strength and an improvement of the creep behaviour leading to a global enhanced performance under monotonic (quasi-static) and probably cyclic loading conditions (remains to be investigated) [19]. Additionally, the costs of the injected material are certainly less expensive, because the shots are a by-product after blasting and occupy about 60% of the injected volume.

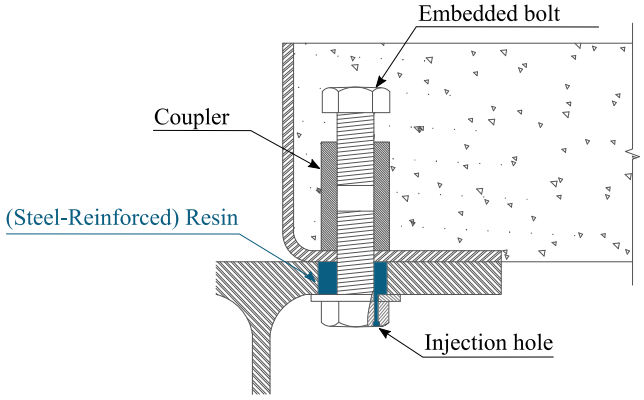

Fig. 1. Resin-injected bolted shear connector for demountable and reusable composite floor systems.
Adapted from [17]

The design of injected bolted connections is typically governed by its long-term behaviour, therefore the characterization of compressive creep properties of injection materials is fundamental. Preliminary tests were made by Nijgh [19] to study the long-term behaviour of injected bolted connections using the same resin as in this paper. Time-dependent deformation was obtained by uniaxial compressive tests on unconfined specimens and the benefit of steel-reinforced resin was evident. However, the complete characterization of creep behaviour of injectants should be conducted using confined specimens.

Nijgh *et al* [20] and Xin *et al* [21] assessed the material response of epoxy resin RenGel® SW 404/ HY2404 and the respective steel-reinforced solution under compressive static loading for both confined and unconfined conditions. However, the thickness of the steel cylinder used to confine resin specimens in those experimental tests was small leading to yielding of the confinement piece which influenced the characterization of the material.

In this paper, compressive material tests on RenGel® SW404/ HY5159 (same base material as used by Nijgh *et al* [20] and Xin *et al* [21] but different hardener) under unconfined/confined conditions are presented. Young's modulus, yield strength and hardening behaviour are obtained from unconfined tests while the stiffness, the residual plastic strain and the viscoelastic strain under confined conditions were assessed using an experimental layout in which specimens are confined with a steel cylinder (its thickness was defined to avoid yielding). Bare resin and steel-reinforced resin specimens are compared. Finite element

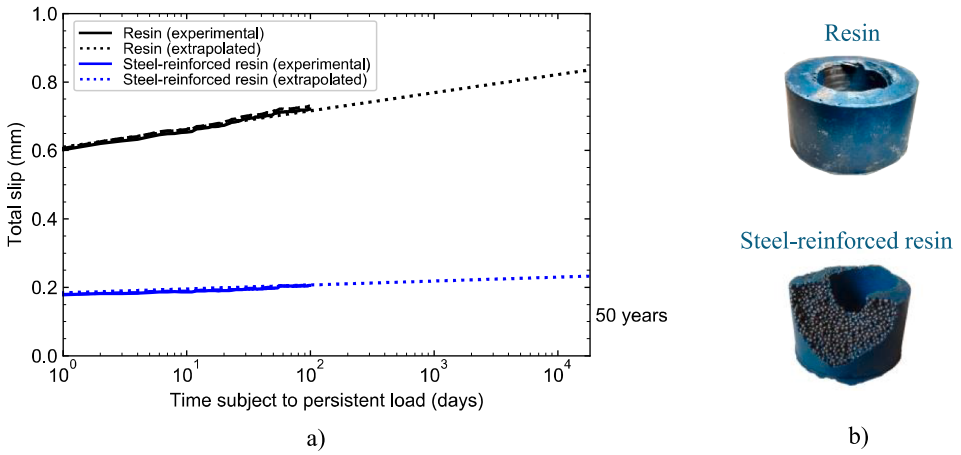

Fig. 2. a) Slip vs. time diagram for a double-lap shear connection with an M20 bolt and a (steel-reinforced) resin-injected oversized hole of Ø32 mm in the centre plate subject to a nominal bearing stress of 175 MPa [16]; b) Injection materials.

simulations of the confined resin and steel-reinforced resin tests were conducted to validate the proposed parameters for the linear Drucker-Prager plastic model. This research intends to be a valuable contribution to numerical assessments and practical design of bolted shear connectors using steel-reinforced resin as injection material.

2. Material model under confined conditions

A constitutive model which includes pressure-dependent behaviour is needed in order to consider the influence of the hydrostatic pressure on the material behaviour as is described in Fig. 3. It ranges from a brittle performance to strain hardening behaviour and material softening does not take place when the hydrostatic pressure is sufficiently high.

The linear Drucker-Prager yield surface [22] represented in the meridional plane (p-t plane) is defined by a straight line as presented in Fig. 4. The equation that defines the yield criterion in the meridional plane is

$$t = d + p\tan\beta \tag{1}$$

where t is the deviatoric stress, p is the hydrostatic pressure, β is the material angle of friction and d is the cohesion of the material defined by (if hardening is defined in compression)

$$d = \left(1 - \frac{1}{3}\tan\beta\right) f_{y,c} \tag{2}$$

where $f_{y,c}$ is the uniaxial compressive yield stress. The deviatoric stress is defined in the equation (3).

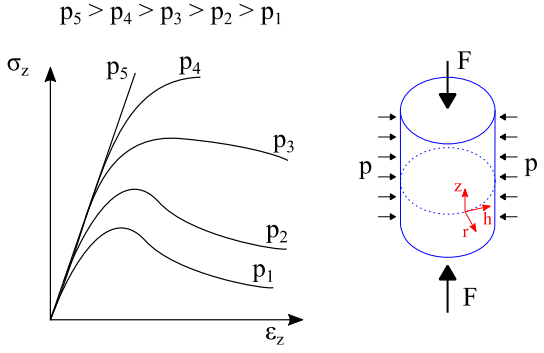

Fig. 3. Schematic material behaviour for different levels of hydrostatic pressure.

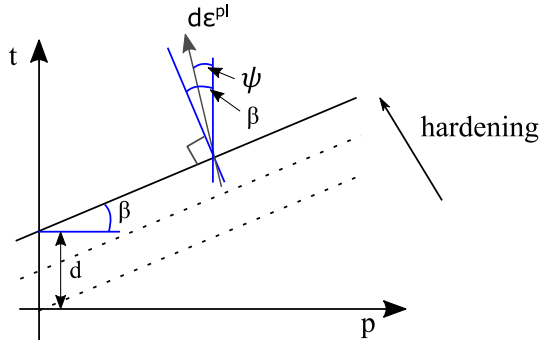

Fig. 4. Linear Drucker-Prager model: yield surface and flow direction in the p(hydrostatic pressure) - t(deviatoric stress) meridional plane [23].

$$t = \frac{q}{2}\left[1 + \frac{1}{K} - \left(1 - \frac{1}{K}\right)\left(\frac{a}{q}\right)^3\right] \tag{3}$$

where q is the von Mises equivalent stress and a is the third invariant of deviatoric stress. Fitting the best straight line through the triaxial compression results provides β and d for the linear Drucker-Prager model. The triaxial compression and tension lines must intercept the p-axis at the same point, and the ratio of values of q for triaxial tension and compression at the same value of p then gives K.

The flow potential of the linear Drucker-Prager model is defined as presented in the following equation:

$$G = t - p\tan\psi \tag{4}$$

where ψ is the dilation angle in the p-t plane. The plastic strain increment $d\varepsilon^{pl}$ is assumed to follow the potential flow rule:

$$d\varepsilon^{pl} = \frac{d\bar{\varepsilon}^{pl}}{c}\frac{\partial G}{\partial \sigma} \tag{5}$$

where c is defined as presented in the following equation (if hardening is defined in uniaxial compression) and $d\bar{\varepsilon}^{pl}$ is the equivalent plastic strain increment.

$$c = \left(1 - \frac{1}{3}\tan\psi\right) \tag{6}$$

If the experimental data is not directly available to obtain the triaxial parameters, the simple way to proceed is to match the Mohr-Coulomb parameters to the Drucker-Prager model. The Mohr-Coulomb failure

model is based on plotting Mohr's circle for states of stress at failure in the plane of the maximum and minimum principal stresses σ_1 and σ_3. This procedure is described in the Abaqus manual [23]. The failure criterion defined by Mohr-Coulomb is given as

$$\frac{\sigma_1 - \sigma_3}{2} = \left[\frac{\sigma_1 + \sigma_3}{2}\right]\sin\varphi + c\cos\varphi \tag{7}$$

which can also be expressed as

$$\sigma_1\frac{(1-\sin\varphi)}{2c\cos\varphi} - \sigma_3\frac{(1+\sin\varphi)}{2c\cos\varphi} = 1 \tag{8}$$

where φ and c represent the angle of internal friction and cohesion, respectively. If the uniaxial tensile and compressive yield stresses are known, the Mohr-Coulomb parameters can be determined as

$$f_{y,t} = \frac{2c\cos\varphi}{1+\sin\varphi} \tag{9}$$

$$f_{y,c} = \frac{2c\cos\varphi}{1-\sin\varphi}. \tag{10}$$

In the case of associated flow (dilatation angle equal to internal friction angle), the parameters of the Drucker-Prager model d and β can be expressed with the Mohr-Coulomb parameters as

$$\tan\beta = \frac{\sqrt{3}\sin\varphi}{\sqrt{1+\frac{1}{3}\sin^2\varphi}} \tag{11}$$

$$\frac{d}{c} = \frac{\sqrt{3}\cos\varphi}{\sqrt{1+\frac{1}{3}\sin^2\varphi}}. \tag{12}$$

The parameter K is determined by

$$K = \frac{3-\sin\varphi}{3+\sin\varphi} \geq 0.778 \tag{13}$$

In this study, the Drucker-Prager parameters were determined by calibrating the numerical results with experimental data.

3. Experimental program

3.1. Unconfined tests

3.1.1. Specimens and materials

A set of specimens was prepared to assess the compressive behaviour at room temperature [19]. The specimens consisted of resin RenGel® SW 404 + HY 5159. It is a two-component epoxy resin with mixing ratio 100:8. Bare resin specimens were used and steel-reinforced resin specimens composed of resin and spherical steel shots produced by J444 standard [24] with 0.8 mm nominal diameter (size class S330) in a loose random packing corresponding to a nominal particle volume fraction of 60%. Three specimens were tested for each material and the geometry of the specimens was φ26 × 50 mm – see Fig. 5. Load was applied under displacement control at a speed of 0.01 mm/s.

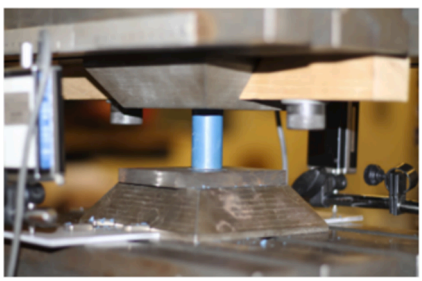

Fig. 5. Experimental set-up for unconfined compression tests [21].

3.1.2. Experimental results

The engineering stress–strain curves for resin and steel-reinforced resin specimens are illustrated in Fig. 6. For resin specimens, the stress–strain curve has four phases: i) linear stress–strain performance; ii) yielding; iii) hardening phase; iv) fracture. The stress–strain curve for steel-reinforced specimens has only two main phases: i) linear stress–-strain performance; ii) fracture.

A set of material parameters obtained from these tests is presented in Table 1. Steel-reinforced resin specimens showed significantly higher Young's moduli (increase of 181%) compared to resin specimens. A significant change in the material behaviour is observed in terms of ductility, since the fracture strain is considerably reduced for steel-reinforced resin. The failure of these brittle specimens was initiated by separation of the resin and the steel particles. For the resin specimens, ductile behaviour was observed and failure was initiated with longitudinal and diagonal cracks until sudden explosive spalling along these cracks. The stress value until which the material shows elastic behaviour has a small increase for steel-reinforced resin of 9.1% when compared to resin specimens.

The Poisson's ratio was found as 0.315 and 0.220 for resin and steel-reinforced resin, respectively. The density of each specimen was determined and the average values were found as 5.26 g/cm^3 for steel-reinforced resin and 1.86 g/cm^3 for resin.

3.2. Confined tests

3.2.1. Experimental setup

Experimental tests were conducted to characterize the material performance of resin under compressive-compressive quasi-static cyclic loading in confined conditions. The test setup – presented in Fig. 7 – includes a cylindrical resin specimen with Φ16mm × 36 mm or a steel-reinforced resin specimen with Φ16mm × 32 mm nominal dimensions. This geometry represents a height nearly 2 times the diameter which is recommended to decrease the influence of friction effects (higher height will lead to higher friction). Smaller specimens will have large variations in internal stresses [25].

The specimens were placed inside a confining steel cylinder whose interior surface was coated with a dicronite layer [26]. Under the specimen was a bearing steel component with Φ15.8 mm and above the specimen there was a loading pin with the same diameter. The gap of 0.1 mm between the pin (and bearing) and the confinement was enough to accommodate the lateral expansion of these components without contact with the confinement.

Resin and steel-reinforced resin used in these experimental tests were the same as used in unconfined tests. Metallic components were produced from structural bolts (steel grade 8.8 for confinement and steel grade 12.9 for loading pin and bearing). A hinge was placed under the

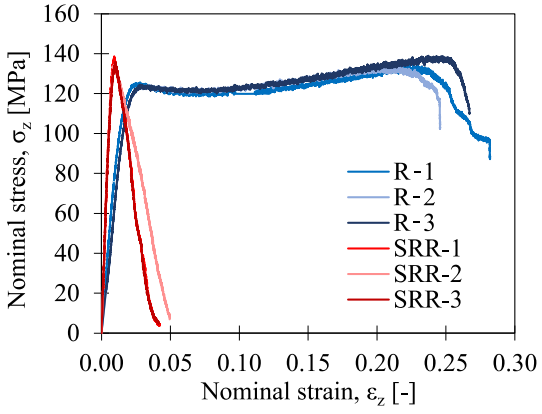

Fig. 6. Nominal stress–strain performance for unconfined resin and steel-reinforced resin specimens.

Table 1
Results for resin and steel-reinforced resin in unconfined tests (nominal values).

Material	Specimen	Young's Modulus	Yield Strength	Fracture Initiation Strain	Fracture Strain
		E_Z [GPa]	$f_{y,c}$ [MPa]	$\varepsilon_{z_0}^f$ [–]	ε_{zu}^f [–]
Resin	R_1	8.6	125.7	0.229	0.282
	R_2	7.5	124.3	0.201	0.246
	R_3	7.4	124.4	0.237	0.267
	Average	7.8	124.8	0.222	0.265
	St. dev.	0.6	0.8	0.019	0.018
Steel-reinforced resin	SRR_1	23.3	138.6	0.009	0.042
	SRR_2	21.8	134.5	0.009	0.049
	SRR_3	20.6	135.8	0.010	0.041
	Average	21.9	136.2	0.010	0.044
	St. dev.	1.3	2.1	0.001	0.004

bearing in order to ensure vertical force flow through the specimen. Linear variable differential transformers were placed to record the displacement between the top of the loading pin and the bottom of the bearing.

Two loading sets were used. In the ascending loading set (A-Set), the specimens were loaded up to 150 kN in 10 steps of 15 kN as represented in Fig. 8a). After unloading in each step, a force of 1–2 kN was maintained for at least 3 min in order to distinguish the viscoelastic from the plastic strain. In the descending loading set (D-Set), the specimens were loaded in 10 consecutive steps in a descending order as presented in Fig. 8b). This loading protocol was defined aiming to evaluate the variation of the material mechanical properties when specimens are subjected to varying load magnitudes.

3.2.2. Ascending set (A-set)

Three resin specimens were tested under A-set. The nominal stress–strain behaviour is presented in Fig. 9a). The first cycle (maximum stress 75 MPa) presents a linear-elastic behaviour while in the second cycle (maximum stress 150 MPa) there is a non-linear performance (stiffness changes). This non-linear behaviour was found in all four tests and it indicates that there was a small difference between the diameter of the specimen and the inner diameter of the confinement piece (inner gap). The specimen reached its yield strength and lateral expansion occur until full confined conditions are reached. In the following cycles (with higher load levels) this phenomenon does not occur and the loading phase is nearly linear.

Each cycle i was analysed separately in order to compute the stiffness of the loading phase and the residual strain. Fig. 9b) represents the analysis conducted for cycle 10 (the last cycle) of specimen A-Set-R1. The regression line of the loading phase is used to compute the stiffness of the material under confined conditions $E_{conf,i}$. Further, the residual strain $\varepsilon_{z,r,i}$ given by the sum of the residual plastic strain $\varepsilon_{z,r,pl,i}$ and the residual viscoelastic strain $\varepsilon_{z,r,visc,i}$ is evaluated per cycle.

Three specimens were produced with steel-reinforced resin and tested under A-Set. Fig. 10 presents the stress–strain behaviour during 10 cycles of loading. The inner gap is also visible for these results since there is a stress plateau in all three tests around 120–135 MPa. From 3rd to 10th cycle, the loading and unloading phases have a constant performance.

The evolution of stiffness for all sets of tests are presented in Fig. 11. For both resin and steel-reinforced resin, the firsts cycles have a similar value to the stiffness obtained in the unconfined test. This shows that

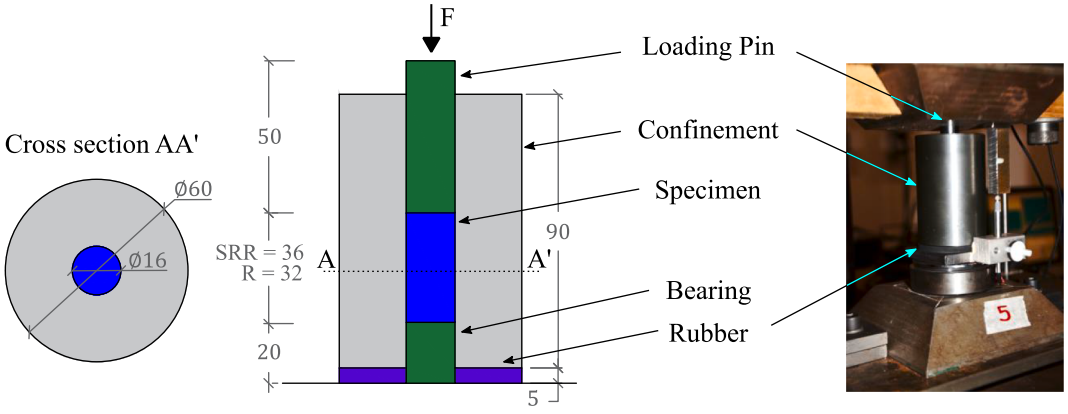

Fig. 7. Experimental setup for confined tests (dimensions in mm).

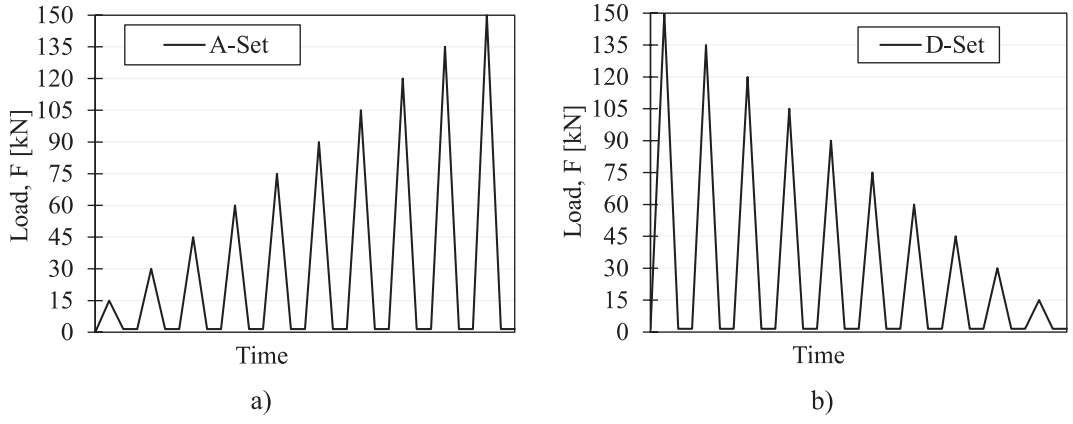

Fig. 8. Schematic quasi-static loading sets: a) Ascending set; b) Descending set.

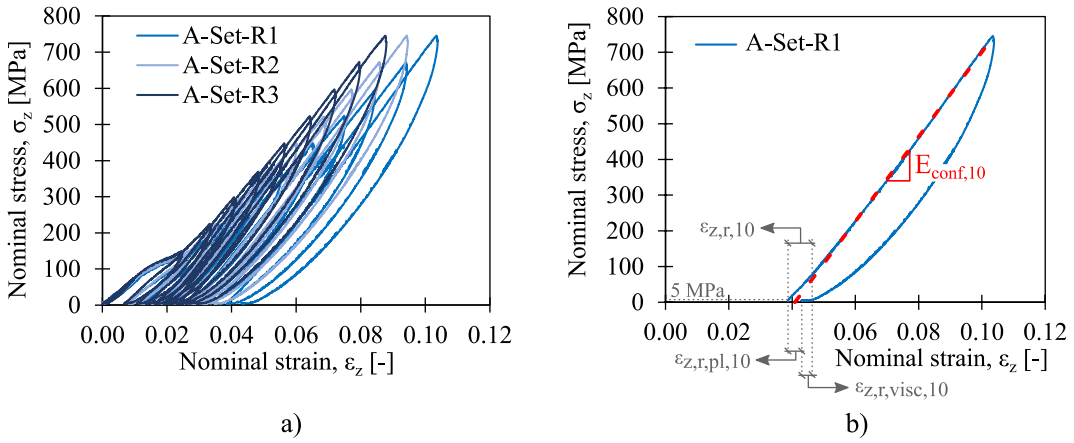

Fig. 9. Resin specimens under A-Set: a) complete stress–strain performance; b) analysis of cycle 10 for specimen A-Set-R1.

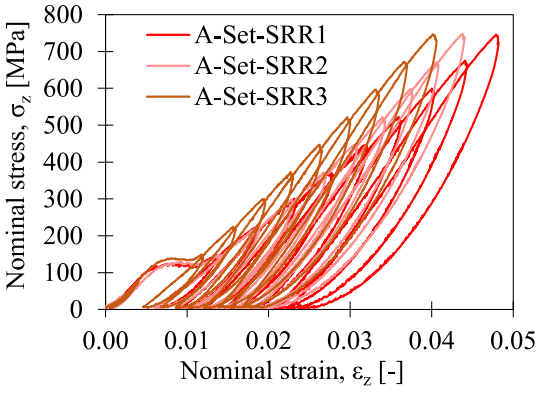

Fig. 10. Steel-reinforced resin specimens under A-Set.

specimens are not in fully confined conditions in first and second cycles. Only after the specimens have expanded laterally and overcome the small gap between specimen and confinement, the behaviour is governed by the confined conditions and the stiffness increases. After these first settling cycles, there is an increase of stiffness in both materials, but while for resin specimens, it stabilizes around 12 GPa after cycle 5, for steel-reinforced resin it increases until the last cycle. This difference can be related to the composite nature of the steel-reinforced solution and to the densification of the material caused by the rearrangement of the steel spheres and filling the voids.

The residual strain $\varepsilon_{z,r,i}$ was computed for every cycle and the results are presented in Fig. 12. The plastic $\varepsilon_{z,r,pl,i}$ and viscoelastic $\varepsilon_{z,r,visc,i}$ components were computed as represented in Fig. 9b). After the first cycle with almost no residual strain (load level under the yield stress of the material), the second cycle has the highest value due to the plastification of specimen and the lateral expansion until the gap between specimen and confinement piece is filled completely. From the second cycle on, the specimens are in fully confined conditions and the residual strain decreases.

Resin specimens exhibited higher residual strains than the steel-reinforced specimens. The presence of steel shots in the steel-reinforced specimens reduces the quantity of resin (the main source of viscosity effects) and consequently the residual strain is lower. From cycle 7 beyond, the average value of viscoelastic strain represents 45% of the total residual strain for both resin and steel-reinforced specimens.

3.2.3. *Descending set (D-set)*

Four tests with resin specimens were performed under D-Set. Nominal stress–strain was computed and the results are presented in Fig. 13. In the first loading step, a non-linear behaviour is obtained, while in subsequent steps the behaviour is mainly linear due to the fully confined conditions. The stiffness computed with the results obtained before the stress plateau is 7.3 GPa which is similar to the value obtained for unconfined solution (7.8 GPa).

For the steel-reinforced material, two specimens were tested in the D-Set. The results can be observed in Fig. 14. In the first cycle (highest load magnitude) there is a significant residual deformation compared to the following cycles due to the same reasons that were given for the resin specimens (settling of the test and transition from unconfined to confined state).

The average stiffness computed before the stress plateau, which occurs at nominal stress around 130 MPa (yield stress), is 18 GPa and similar to unconfined result (19 GPa). After yielding and the lateral expansion of the specimen in the stress plateau, a nearly linear

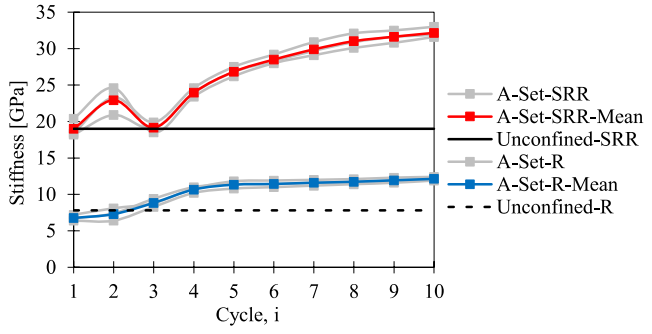

Fig. 11. Development of the stiffness for steel and steel-reinforced resin specimens: A-Set.

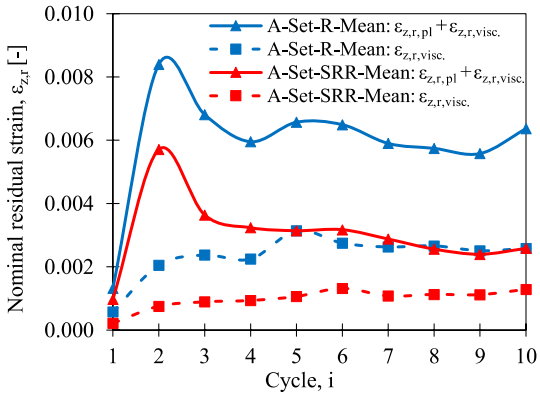

Fig. 12. Residual strain for resin and steel-reinforced resin specimens: A-Set.

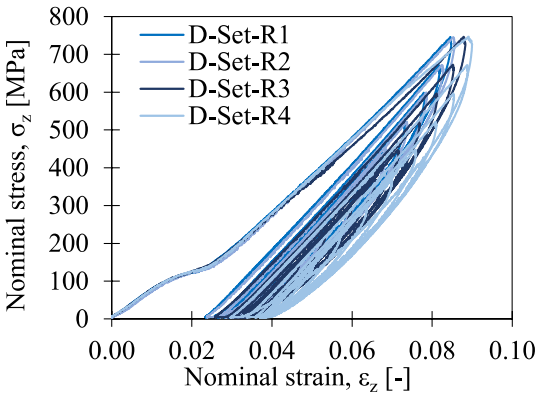

Fig. 13. Resin specimens under D-Set.

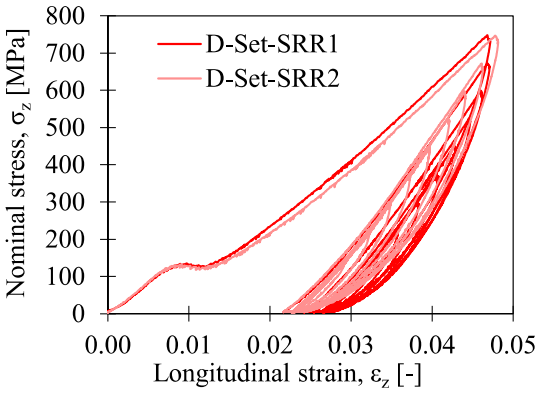

Fig. 14. Steel-reinforced resin specimens under D-Set.

performance is observed until the maximum stress is reached. This linearity is maintained in the following cycles.

The value found for the stiffness for each cycle is presented in Fig. 15. The stiffness of the first cycle (computed for the results after the stress plateau) is closer to the value for unconfined conditions. Even if confined conditions are achieved, in this first cycle the specimen is in a settling process in which voids are compressed. The difference between first and second cycle is more significant for steel-reinforced material which can be attributed to its composite nature and densification of the steel shots matrix. For resin specimen, from the second cycle beyond, the value of stiffness stabilizes around 11.5 GPa and in the final step, in which the load magnitude is below the yield stress of the material, the stiffness has a small decrease of 1 GPa which can be explained by not fully confined conditions. For steel-reinforced resin specimens, after the first cycle the material gets denser with the value of the stiffness increasing significantly; then it is nearly constant until cycle 8. In the last

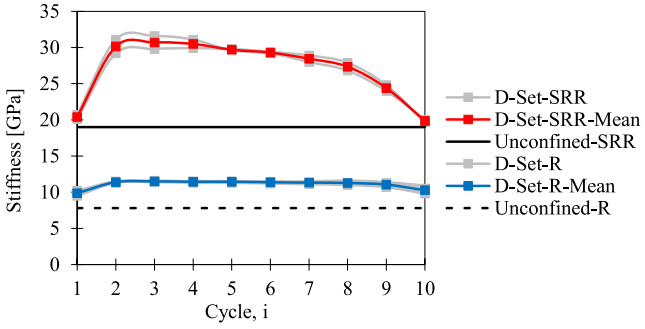

Fig. 15. Stiffness evolution for steel and steel-reinforced resin specimens: D-Set.

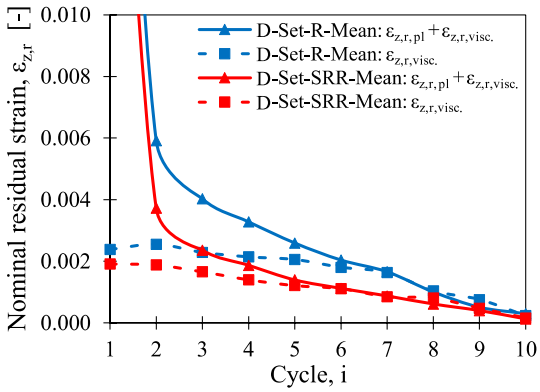

Fig. 16. Residual strain for resin and steel-reinforced resin specimens: D-Set.

two cycles, the applied load level is smaller, the specimens return to not fully confined conditions and the stiffness decreases to near the unconfined solution.

The analysis of residual strain is presented in Fig. 16 showing that resin specimens present higher total residual strain values in all cycles compared to steel-reinforced resin specimen. The first cycle (with higher load) has a higher residual strain comparing to the following cycles which is caused by the settling process and transition between unconfined to confined state. From cycle 5 on, the percentage of viscoelastic strain is always superior to 90% of the total residual strain.

3.2.4. *Summary of results*

These experimental tests allow to define the material properties of resin and steel-reinforced resin specimens under unconfined and confined conditions:

- From the unconfined tests it was found that using a steel matrix together with an epoxy resin influenced the stiffness and ductility. Then Young's modulus increased by 181% and the fracture strain for steel-reinforced solution is 17% of the value found for bare resin specimens. The yield stress was not significantly changed which means that it is mainly influenced by the resin material.
- The experimental setup defined for confined tests was efficient to test specimens under confined conditions after the first cycles.
- Both materials present a linear behaviour on loading phase under confined conditions. Stiffness in confined conditions is 148% and 157% higher than in unconfined conditions for resin and steel-reinforced resin material, respectively – see Table 2.
- Under confined conditions, after 10 cycles the stiffness of steel-reinforced specimens is around 2.6 times higher than the stiffness of resin specimens;
- After the initial settling, the stiffness for resin specimens does not vary when the specimen is in confined conditions; however, for steel-reinforced specimens the stiffness increases due to the densification of the material;
- When using steel shots and fewer resin (steel-reinforced solution), the residual plastic strain and viscoelastic strain are decreased which is caused by the different Young's moduli and hardening behaviours; This reduction on material strain will contribute to reduce the slip at the connection level.

Table 2
Stiffness of resin and unconfined resin materials.

Resin			Steel-reinforced resin		
Confined		Unconfined	Confined		Unconfined
A-Set	11.7 GPa	7.8 GPa	A-Set	30.0 GPa	21.9 GPa
D-Set	11.4 GPa		D-Set	29.5 GPa	

- Scatter on results is higher for steel-reinforced resin due to material heterogeneities.

4. Numerical simulation of the material experiments

4.1. Model setup

A 3D finite element model of the experimental setup was developed using ABAQUS 2020 – see Fig. 17 – using C3D8R finite elements [23]. The maximum element size was 1 mm. The load was applied on top of loading pin in ZZ direction and all translation degrees of freedom on the bottom surface of the bearing piece were fixed. Contact between the components was defined with the surface-to-surface contact methodology based on tangential and normal behaviour. The friction coefficient between specimens and the surrounding elements (confinement, loading pin and bearing) was set as 0.075 and 0.350 for resin and steel-reinforced resin specimens, respectively. When steel-reinforced resin specimens are used, the value of the friction coefficient is increased due to the presence of the steel shots. Since specimens are in unconfined state at the beginning of the test due to small differences in diameter of the specimen and the inner circle of the confinement piece, it was decided to model a gap between the specimen and the confinement piece of 0.1 mm.

4.2. Material properties

All metallic components (loading pin, bearing and confinement piece) were modelled using a linear model with 210 GPa of Young's modulus and 0.3 for Poisson's coefficient. The material model used for the specimens was based on elastic parameters, hardening performance (see Table 3) and Drucker-Prager yield criterion.

The implementation of the Drucker-Prager model depends mainly on the internal friction angle φ. It influences the shape of the stress–strain curve during the loading phase and the residual plastic strain. The parameters of the linear Drucker-Prager model for resin and steel-reinforced resin were defined by calibration with the experimental results. Their values are presented in Table 4.

4.3. Numerical results

The numerical computation for resin and steel-reinforced resin specimens under the ascending and descending loading sets were conducted. Longitudinal (zz-direction) deformation, von Mises stresses and radial deformation at maximum applied load of cycle 10 are presented in Fig. 18a), b) and c), respectively.

The correlation between numerical and experimental results of the longitudinal nominal stresses and strains for cycle 2 of A-Set is presented in Fig. 19. This is the cycle where the stress plateau occurs. In these

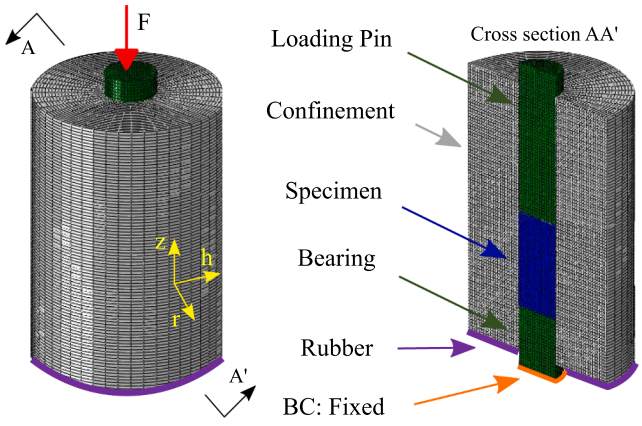

Fig. 17. Finite element model of confined material test.

Table 3
Hardening law for resin and steel-reinforced resin.

Resin		Steel-reinforced resin	
True stress σ_z [MPa]	True plastic strain $\varepsilon_{z,pl}$ [–]	True stress σ_z [MPa]	True plastic strain $\varepsilon_{z,pl}$ [–]
125.0	0.0000	135.0	0.0000
120.0	0.0115	136.2	0.0039
115.0	0.0395	130.0	0.0074
110.0	0.0895	100.0	0.0154
106.0	0.1895	20.0	0.0354

Table 4
Parameters to define Drucker-Prager model.

	φ [°]	c [MPa]	β [°]	K [–]	ψ [°]
Resin	25.0	39.8	35.42	0.778	35.42
Steel-reinforced resin	65.0	21.7	54.28	0.778	54.28

figures, all data is translated to zero strain coordinates considering the linear regression defined to compute the stiffness of the loading phase. The numerical model can efficiently predict the stress plateau observed in cycle 2. In Fig. 20, the same comparison is established but in this case for cycle 10. It shows that the behaviour is linear during the loading phase and the numerical results correlate with the experimental evidences.

The radial deformation at the maximum applied load of each cycle of the A-Set was computed over the length of the specimen – see Fig. 18c). For both resin and steel-reinforced resin specimens, the results are presented in Fig. 21. In the first cycle, the radial deformation is higher in the middle of the specimen for both materials but the maximum value for steel-reinforced resin represents 29% of the value found for resin specimens. Both specimens are in unconfined conditions during the first cycle. In the second cycle, the resin specimen is almost completely in confined conditions since the radial deformation is 0.1 mm for nearly all its length, however for the steel-reinforced resin, only a small region in the middle of the specimen reached confined state. This difference is related to its higher stiffness. For the first and second cycles, radial deformation has a symmetrical shape over the length of the specimen, but in the following cycles the values are higher at the upper part of the specimen, near the loading pin. This effect is attributed to the friction forces which are developed when the specimen is in contact with the confinement piece. The radial deformation in the last cycles is higher for the resin specimens which is attributed to its lower stiffness and higher Poisson coefficient.

The radial deformation for resin and steel-reinforced resin specimens under the D-Set are presented in Fig. 22. In this loading case in which the first cycle has the highest load, specimens are in fully confined conditions during the entire test and a non-symmetrical distribution of radial deformation is evident from the first cycle and beyond. Since the central part of the specimen gets in contact with the confined piece in a first stage, the friction forces start to be developed in that region originating higher radial deformation in the upper part of the specimen. The resin specimens present higher radial deformations as in the previous loading set due to its material properties. Steel-reinforced resin specimens show peaks of radial deformation near to the edges which is related to higher friction forces developed in that region.

The longitudinal true stresses over the length of the specimen at maximum load of each cycle for the A-Set are presented in Fig. 23. The first cycles present a nearly constant value since the specimens are in unconfined conditions. In the following cycles, the longitudinal stresses have a non-uniform distribution over the length, since the specimens get in contact with the confinement piece and friction forces are developed. It is evident that higher stresses are developed in the upper part of the specimen in which the load is applied and friction forces are more

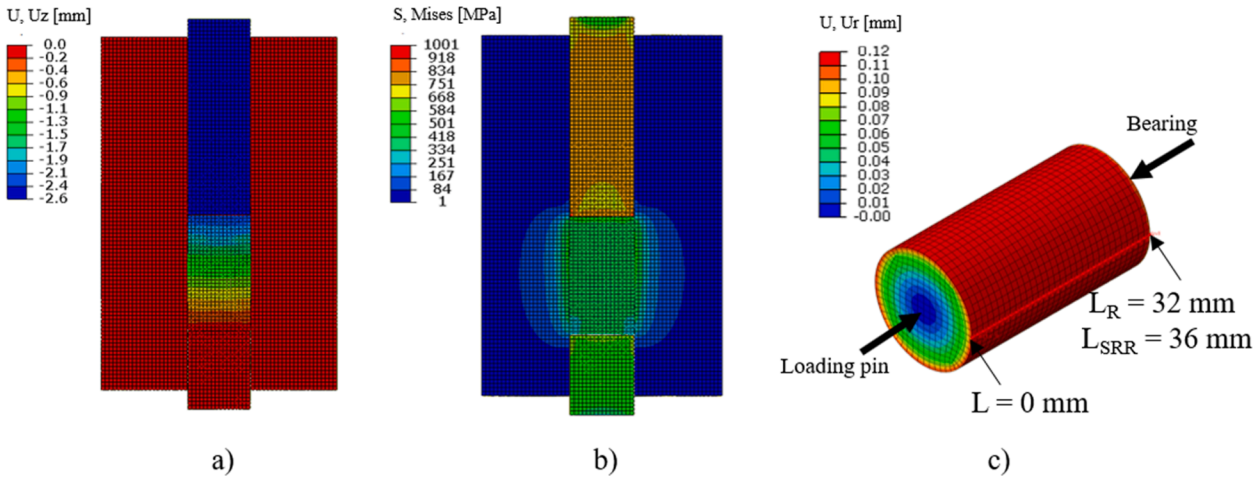

Fig. 18. Numerical results for **resin** specimen (**A-Set**) at maximum applied load of cycle 10: a) longitudinal deformation; b) von Mises stresses; c) radial deformation.

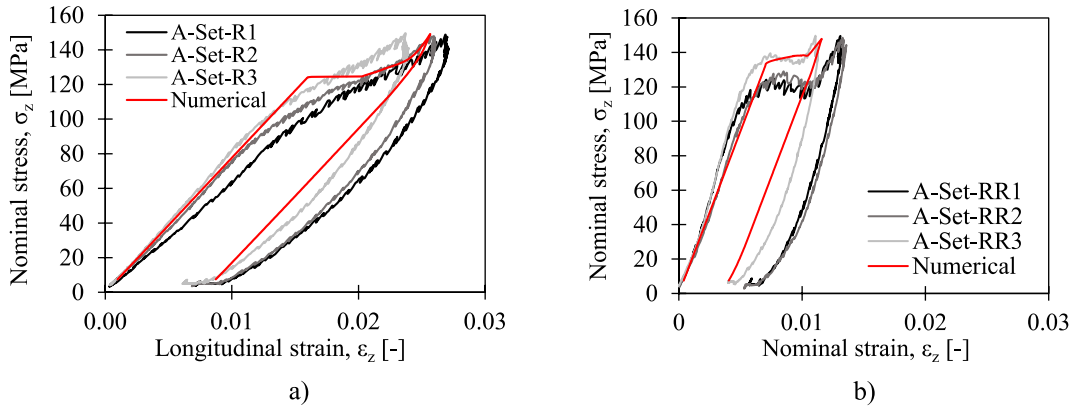

Fig. 19. Numerical and experimental stress–strain for **cycle 2** of **A-set**: a) resin; b) steel-reinforced resin.

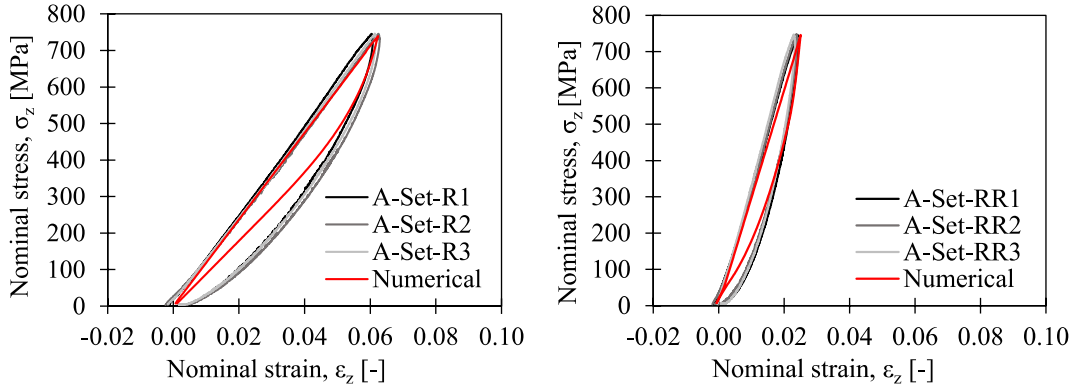

Fig. 20. Numerical and experimental stress–strain for **cycle 10** of **A-set**: a) resin; b) steel-reinforced resin.

relevant. The difference between top and bottom longitudinal stresses is more significant for steel-reinforced specimens mainly due to higher friction forces that are developed.

The longitudinal true stresses under the D-Set are presented in Fig. 24. They show a reversed, yet very similar performance to longitudinal stresses computed for A-Set. Friction forces are higher in the upper part of the specimen leading to higher stresses in that region. A non-uniform distribution of the stresses is evident from the first load cycle.

Finally, the value of the stiffness obtained by numerical analysis is compared with experimental results. In Fig. 25a), it is possible to observe a good agreement for resin specimens in A-set and D-Set. In the case of steel-reinforced resin, a comparison is established in Fig. 25b).

In the A-Set, from cycle 1 to cycle 3, the numerical results are coherent with the experimental results by presenting a stiffness similar to the stiffness found for the unconfined solution. Reaching cycle 5, the stiffness stabilizes around 30 GPa which is very well correlated with the experimental results. For the D-Set, excluding cycle 1 which is affected by settling of the specimen, there is a good agreement between the numerical and experimental results. The numerical model is able to

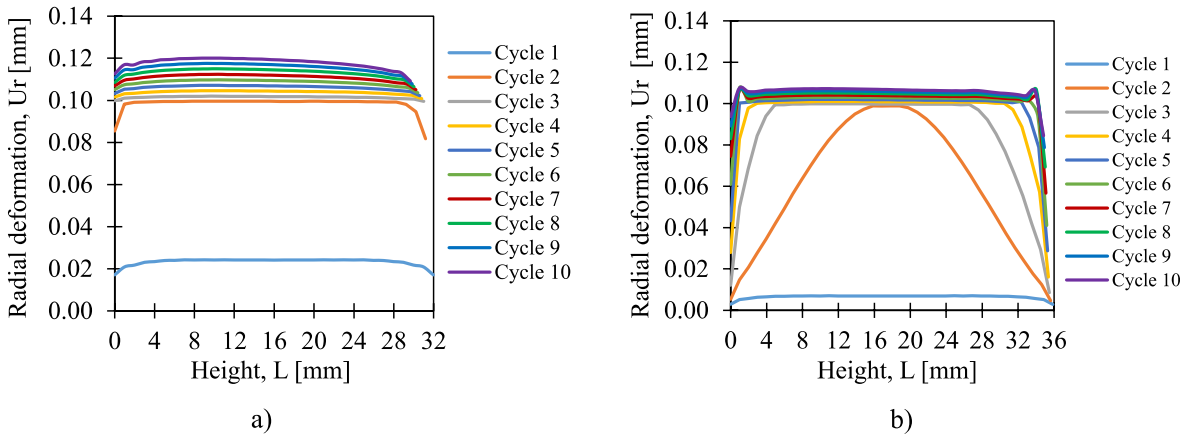

Fig. 21. Radial deformation at maximum load of each cycle for **A-Set**: a) resin; b) steel-reinforced resin.

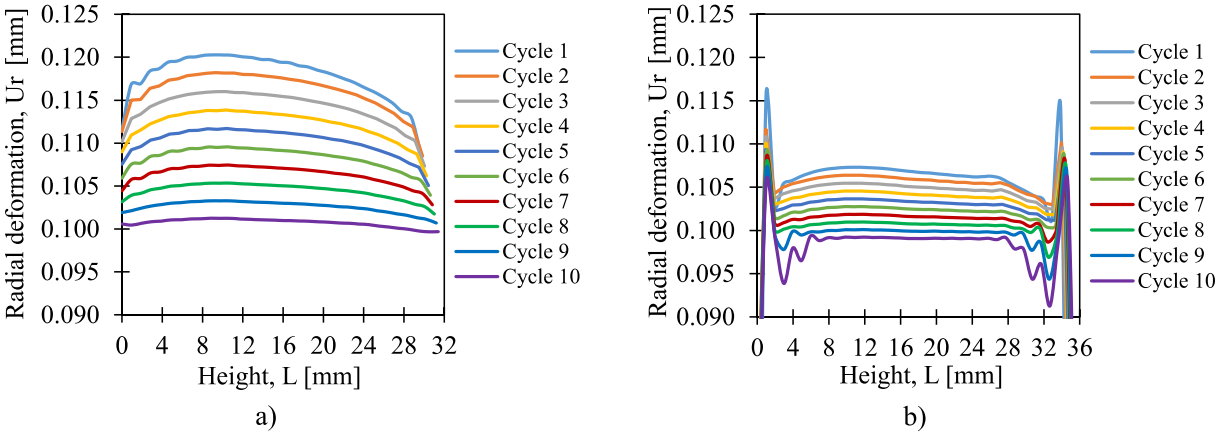

Fig. 22. Radial deformation at maximum load of each cycle for **D-Set**: a) resin; b) steel-reinforced resin.

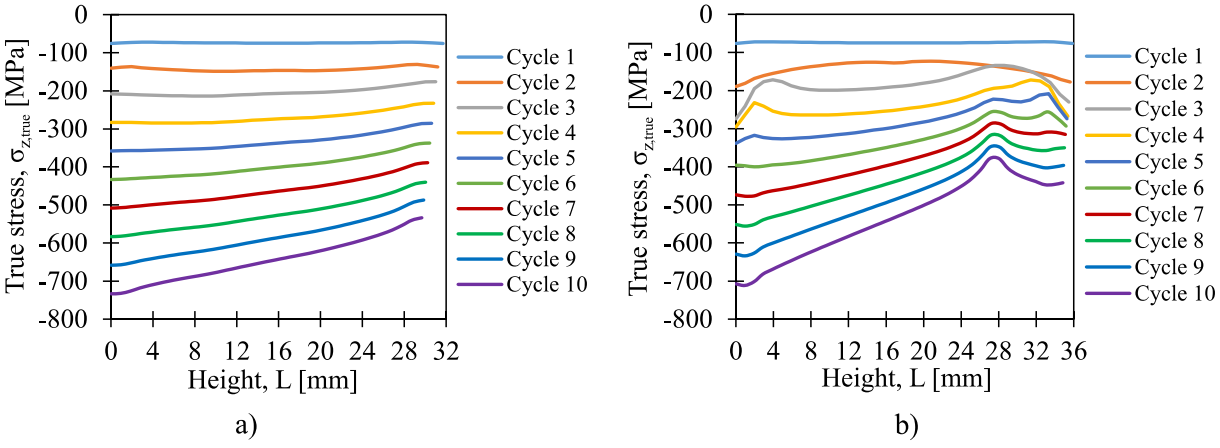

Fig. 23. Longitudinal stresses at maximum load of each cycle for **A-Set**: a) resin; b) steel-reinforced resin.

predict the loss of stiffness in the last two cycles due to partially confined conditions. This effect is more evident for steel-reinforced specimens because the residual strains are considerably lower when compared to resin specimens.

5. Conclusions

Experimental results were obtained using unconfined and confined compressive tests of bare resin specimens and steel-reinforced resin specimens and used to validate numerical material models.

The unconfined results allowed to define uniaxial material properties, such as the Young's modulus, Poisson coefficient and hardening/softening behaviour [19]. Steel-reinforced resin led to 1.81 times higher stiffness and a significant reduction of the strain at failure.

When confined, the steel-reinforced specimens provide a constant increase in stiffness after the specimen's settlement due to the densification of material while the resin specimens showed a constant value. In the last cycle, the steel-reinforced resin specimens have 2.6 times higher

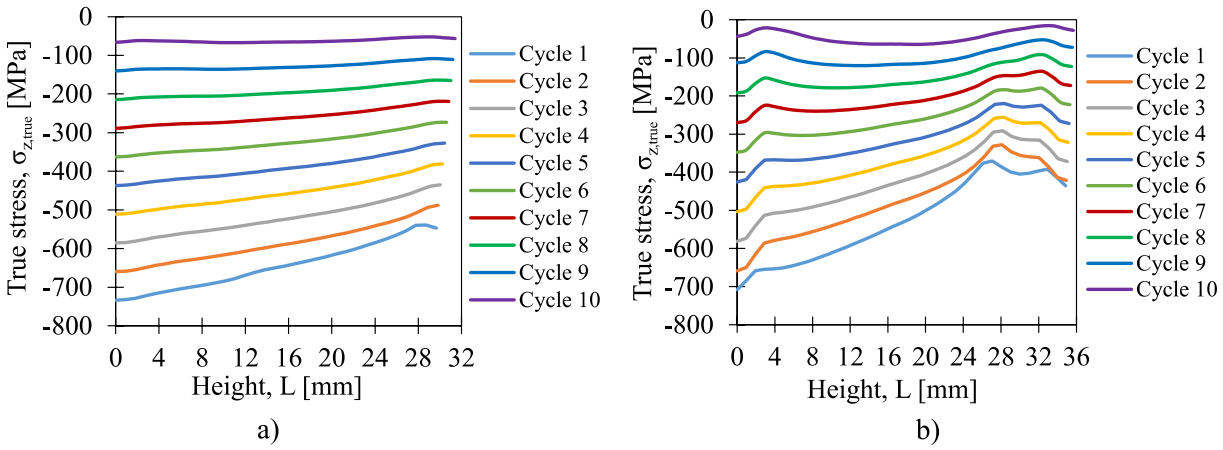

Fig. 24. Longitudinal stresses at maximum load of each cycle for **D-Set**: a) resin; b) steel-reinforced resin.

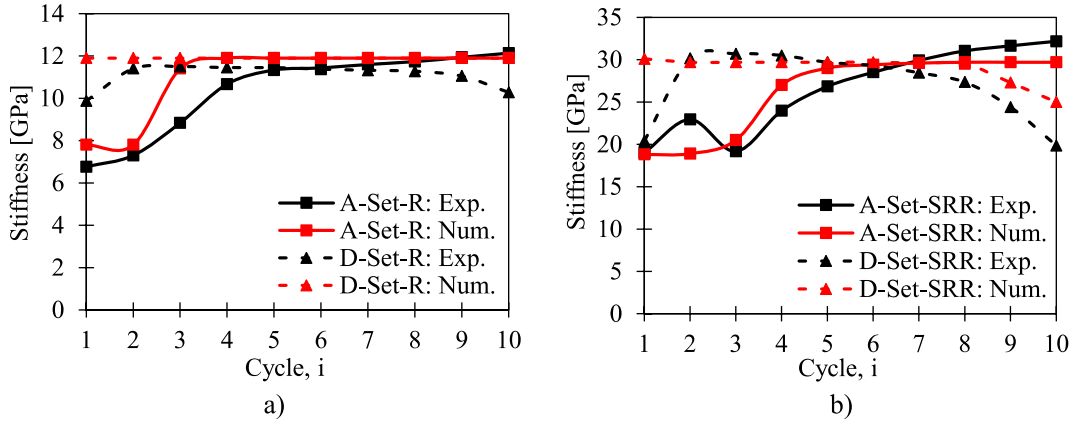

Fig. 25. Numerical and experimental stiffness: a) resin specimens; b) steel-reinforced resin specimens.

stiffness comparing to bare resin specimens. Furthermore, the steel-reinforced solution presented lower strains – both viscoelastic and residual plastic strains – which would lead to a reduction of slip at the connection level.

The experimental setup was successful in achieving confined conditions, as the cylinder did not yield. However, the geometry of the (steel-reinforced) resin body in a shear connector will result in a more complex stress distribution due to the possibility of the injection material to flow around the bolt shank when in service which requires additional investigation. Furthermore, future research should be focused also on the long-term behaviour of these materials, especially in what concerns its creep performance.

The behaviour of the two materials under confined conditions was efficiently described using the linear Drucker-Prager plastic model implemented in a finite element simulation. The friction angle, the ratio of the yield stress in triaxial tension to the yield stress in triaxial compression and the dilation angle were obtained based on experimental and numerical homogenization. The effect of the lateral confinement was successfully considered by combining Drucker-Prager parameters and the unconfined experimental results.

A summary of the proposed material properties based on the experimental and numerical work is presented in Appendix A. The higher stiffness of steel-reinforced resin compared to bare resin material is fundamental to achieve slip-resistant connections. The definition of material models under confined conditions developed in this paper can be used to perform efficient numerical modelling of bolted shear connectors.

CRediT authorship contribution statement

Bruno Pedrosa: Methodology, Validation, Investigation, Writing – original draft. **Linda Bücking:** Methodology, Validation, Investigation, Writing – review & editing. **Milan Veljkovic:** Conceptualization, Validation, Writing – review & editing.

Declaration of Competing Interest

The authors declare that they have no known competing financial interests or personal relationships that could have appeared to influence the work reported in this paper.

Acknowledgements

The authors would like to acknowledge the Fundação para a Ciência e Tecnologia (FCT) for funding the Ph.D. scholarship SFRH/BD/145037/2019.

Appendix A. Material properties

Property		Resin		Steel-reinforced resin	
Components		RenGel® SW 404 + Ren© HY 5159		[RenGel® SW 404 + Ren© HY 5159] + Steel shots	
Density [g/cm^3]		1.86		5.26	
Poisson's ratio [–]		0.315		0.220	
Stiffness [GPa]	Unconfined	7.8		21.9	
	Confined	11.6		29.8	
Drucker-Prager model	φ[°]	25		65	
	c[MPa]	39.8		21.7	
	β [°]	35.42		54.28	
	K [–]	0.778		0.778	
	ψ [°]	35.42		54.28	
Hardening law		True stress [MPa]	True plastic strain [–]	True stress [MPa]	True plastic strain [–]
		125.0	0.0000	135.0	0.0000
		120.0	0.0115	136.2	0.0039
		115.0	0.0395	130.0	0.0074
		110.0	0.0895	100.0	0.0154
		106.0	0.1895	20.0	0.0354

References

[1] Gresnigt A, Sedlacek G, Paschen M. Injection bolts to repair old bridges. Proceedings of Connections in Steel Structures IV 2000.
[2] CEN. EN 1090-2. Execution of steel structures and aluminium structures – Part 2: Technical requirements for steel structures. European Committee for Standardization, 2008.
[3] European recommendations for bolted connections with injection bolts. Publication No 79; 1994.
[4] Kortiš I. The numerical solution of the bolted connection with the low-quality injected bolts. In: Proceedings of 9th International Conference on New Trends in Statics and Dynamics of Buildings, Bratislava; 2011.
[5] CEN. EN 1993-1-8: Eurocode 3, Design of steel structures – Part 1-8: Design of joints. Brussels: European Committee for Standardization; 2005.
[6] Rijkswaterstaat Steunpunt Opdrachtgeversschap. Eisen voor voegovergangen. Tech. Rep. 2007.
[7] Gresnigt A, Beg D. Design bearing stresses for injection bolts with short and long duration high loads. Proceedings of the Fifth International Conference on Structural Engineering,Mechanics and Computation 2013:1317–22.
[8] Olivier G, Csillag F, Tromp E, Pavlović M. Conventional vs. reinforced resin injected connectors' behaviour in static, fatigue and creep experiments on slip-resistant steel-FRP joints. Engineering Structures 2021;236:112089. https://doi.org/10.1016/j.engstruct.2021.112089.
[9] Olivier G, Csillag F, Tromp E, Pavlović M. Static, fatigue and creep performance of blind-bolted connectors in shear experiments on steel-FRP joints. Engineering Structures 2021;230:111713. https://doi.org/10.1016/j.engstruct.2020.111713.
[10] Csillag F, Pavlović M. Push-out behaviour of demountable injected vs. blind-bolted connectors in FRP decks. Composite Structures 2021;270:114043. https://doi.org/10.1016/j.compstruct.2021.114043.
[11] Gresnight A, Stark J. Design of bolted connection with injection bolts. Proceedings from the Third International Workshop on Connections in Steel Structures: Behaviour, Strength and Design 1996:77–87.
[12] Pedrosa B, Correia J, Rebelo C, Veljkovic M, Gervásio H. Fatigue experimental characterization of preloaded injection bolts in a metallic bridge strengthening scenario. Engineering Structures 2021;234:112005. https://doi.org/10.1016/j.engstruct.2021.112005.
[13] van Wingerde A, van Delft D, Knudsen E. Fatigue behaviour of bolted connections in pultruded FRP profiles. Plastics, Rubber and Composites 2003;32(2):71–6.
[14] Correia J, Pedrosa B, Raposo P, De Jesus A, Gervásio H, Lesiuk G, et al. Fatigue strength evaluation of resin-injected bolted connections using statistical analysis. Engineering 2017;3(6):795–805.
[15] Pedrosa B, Rebelo C, Gervásio H, Silva L, Correia J. Fatigue of Preloaded Bolted Connections with Injection Bolts. Structural Engineering International 2020;30(1):102–8.
[16] Nijgh M, Veljkovic M. Requirements for oversized holes for reusable steel-concrete composite floor systems. Structures 2020;24:489–98.
[17] Nijgh M, Girbacea I, Veljkovic M. Elastic behaviour of a tapered steel-concrete composite beam optimized for reuse. Engineering Structures 2019;183:366–74. https://doi.org/10.1016/j.engstruct.2019.01.022.
[18] Nijgh M. New materials for injected bolted connections – a feasibility study for demountable connections. Delft University of Technology; 2017. MSc Thesis.
[19] Nijgh M. A multi-scale approach towards reusable steel-concrete composite floor systems. Delft University of Technology; 2021. PhD Thesis.
[20] Nijgh M, Xin H, Veljkovic M. Non-linear hybrid homogenization method for steel-reinforced resin. Construction and Building Materials 2018;182:324–33.
[21] Xin H, Nijgh M, Veljkovic M. Computational homogenization simulation on steel reinforced resin used in the injected bolted connections. Composite Structures 2019;210:942–57.
[22] Drucker DC, Prager W. Soil mechanics and plastic analysis or limit design. Quarterly of Applied Mathematics 1952;10(2):157–65.
[23] Hibbit D, Karlsson B, Sorensen P. ABAQUS/standard user's manual, Ver. 6.10. Pawtucket, Rhode Island; 2004.
[24] SAE. J444 – Cast shot and grit size specifications for peening and cleaning; 2012.
[25] Ravi-Chandar K, Ma Z. Inelastic deformation in polymers under multiaxial compression. Mechanics of Time-Dependent Materials 2000;4:333–57.
[26] CZL Tilburg bv; n.d. https://www.czltilburg.nl/nl/processen/dicronite-dry-lubrication\.